Research Article

Adaptively Active Contours Based on Variable Exponent $L^{p(|\nabla I|)}$ Norm for Image Segmentation

Wenying Wen,[1] Chuanjiang He,[1] Meng Li,[2,3] and Yi Zhan[4]

[1] College of Mathematics and Statistics, Chongqing University, Chongqing 400044, China
[2] School of Mathematics and Finances, Chongqing University of Arts and Sciences, Chongqing 402160, China
[3] Key Laboratory of Data Analyzing and Image Processing, Chongqing University of Arts and Sciences, Chongqing 402160, China
[4] College of Mathematics and Statistics, Chongqing Technology and Business University, Chongqing 400067, China

Correspondence should be addressed to Wenying Wen, wenwenying20071060@yahoo.com.cn

We propose an $L^{p(|\nabla I|)}$-based adaptively active contours model for image segmentation which is derived from the well-known Chan-Vese (C-V) model. Unlike the C-V model, the proposed model uses the $L^{p(|\nabla I|)}$ ($p(|\nabla I|) > 2$) norm instead of the L^2 norm to define the external energy and incorporates an extra internal energy into the overall energy. Due to the variable exponent $p(|\nabla I|)$ which could fit the image gradient information adaptively, the proposed $L^{p(|\nabla I|)}$-based model has the hope of segmenting those images with low contrast and blurred boundaries. Experimental results show that the proposed model with $p(|\nabla I|) > 2$ really can effectively and quickly segment those images with low contrast and blurred boundaries.

1. Introduction

Image segmentation has always been an essential problem in image analysis and computer vision. Segmentation is the process of partitioning an image into a set of distinct regions, each of which has a consistent trait (intensity, etc.) that is different from other regions in the image. Its goal is to change the representation of an image into something that is more meaningful and easier to analyze. So far, a large number of efficient algorithms and methodologies including active contour models have been proposed for image segmentation. In this study, we focus on implicit active contour models [1], that is, active contour models in a level set formulation.

Implicit active contour models, which are implemented via curve evolution theory [2] and level set method [3], have been proved to be an efficient framework for image

segmentation. The basic idea is that an active contour is implicitly represented as the zero level set of a level set function defined in image domain, and then the level set function is deformed according to an evolution partial differential equation (PDE). A remarkable merit of implicit models is that the level set function evolution allows for cusps, corners, and automatic topological change of active contour, which is generally impossible in traditional parametric active contours [4] when direct implementations are performed. Early implicit models [5, 6] first yield an evolution PDE of a parametrized contour, and then convert it to the evolution PDE for a level set function whose zero level set represents the parametrized contour. Alternatively, the evolution PDE for level set function can be directly derived from the minimization problem for an energy functional that takes a level set function rather than a curve as its argument by steepest descent [7–17].

Existing implicit active contour models can be roughly categorized into two basic classes: edge-based models [5–10], and region-based models [11–20]. Edge-based models utilize typically image gradient as an external force to attract the contour towards the boundaries of the desired objects. They have been successfully used to segment images with strong object boundaries defined by gradient, but they have difficulty in handling images with weak boundaries. Region-based models usually utilize region information rather than the gradients on the boundaries to perform segmentation; therefore, they generally have better performance than the former in the presence of weak object boundaries. In addition, region-based models are significantly less sensitive to the location of initial contours. One of the most popular region-based models is the two-phase piecewise constant segmentation model (usually called C-V model) proposed by Chan and Vese [11].

The C-V model relies fully on the global information of image instead of its local gradient. It can realize the global optimization of image segmentation through the minimization of Mumford-Shah energy functional [21], and thus works well on images with roughly constant foreground and background. But for more general images, such as images with low contrast and blurred boundaries, the C-V model shares the lower speed, and even fails to segment.

To address general images, some more sophisticated models than the C-V model have been proposed. For example, Li et al. [12] proposed recently the region-scalable fitting (usually called RSF) active contour model. However, the RSF model is presented to handle intensity inhomogeneity, and it is sensitive to the location of initial contours and needs time-consuming convolution operations. To increase the segmentation speed, Bresson et al. [18] proposed a fast global minimization based on a dual formulation of the active contour/snake model; Chan et al. [19] proposed the algorithm for finding global minimizers of image segmentation; Goldstein et al. [20] proposed the Split Bregman Method for globally convex segmentation model. These works [18–20] represent the state-of-the-art of contour evolution methods which are efficient and fast in a global minimization framework, and they have been widely used in practical application. However, for some images with low contrast and blurred boundaries, these models also seem powerless.

In order to handle those images efficiently and quickly, our idea is to introduce a much simpler model which has many desirable properties as the model introduced in [11] and is efficient in numerical computation. In this study, we propose an improved active contours model based on $L^{p(|\nabla I|)}(p(|\nabla I|) > 2)$ norm instead of the L^2 norm to define the external energy, and incorporate an extra internal energy into the overall energy. The proposed model has the following two advantages. Firstly, the proposed model shares the advantages of the C-V model, such as the robustness to noise and the location of initial contours, and it leads itself particularly well and very fast to the segmentation of those images that the C-V model

can handle. Secondly, the proposed model based on $L^{p(|\nabla I|)}$ norm combines the gradient information with the region information, so it has the hope of segmenting those images with low contrast and blurred boundaries.

The remainder of this paper is organized as follows. Section 2 briefly reviews the C-V model. Section 3 introduces the proposed model. Section 4 presents numerical algorithm and experimental results for some synthetic and real images, followed by the discussion about the parameter used in the segmentation algorithm in Section 5. This paper is summarized in Section 6.

2. The C-V Model

2.1. Minimal Partition Problem

Given an observed image $I : \Omega \subset R^2 \rightarrow R$, the general Mumford-Shah functional [21] for image segmentation is given by

$$E^{\mathrm{MS}}(u, C) = \int_{\Omega} (u - I)^2 dxdy + v \int_{\Omega \backslash C} |\nabla u|^2 dxdy + \mu|C|. \tag{2.1}$$

In the above, $v, \mu > 0$ are fixed scale parameters, u is an unknown piecewise smooth approximation of I, C is an unknown curve, $|C|$ is the length of C, and $\Omega \setminus C$ are the domain excluding the curve C. Mumford and Shah [21] proposed that the segmentation of an image can be obtained by minimizing the functional (2.1).

In order to obtain an optimal piecewise-constant approximation of the image I, Mumford and Shah [21] proposed the following minimal partition problem: given an image $I : \Omega \rightarrow R$, find a set of disjoint regions Ω_i, such that $u = c_i$ in each Ω_i is a minimizer of the following functional, a special case of the functional (2.1):

$$E^{\mathrm{PC}}(u, C) = \sum_i \int_{\Omega_i} |I(x, y) - c_i|^2 dxdy + v|C|, \tag{2.2}$$

where $C = \cup \partial \Omega_i$, $\Omega = \cup \Omega_i \cup C$. In practice, it is not a trivial task to minimize the functional (2.2) due to the unknown contour C of lower dimension and the nonconvexity of the functional. The existence and regularity for the piecewise constant model have been proved in the book [22].

2.2. The C-V Model

In [11], Chan and Vese solved a particular case of the minimal partition problem (2.2) for image segmentation using the curve evolution and the level set method, where the binary case of two regions was considered. Based on (2.2) and using the level set method, Chan and Vese proposed to minimize the following functional for a two-phase segmentation:

$$E(c_1, c_2, \phi) = \int_{\Omega} |I - c_1|^2 H(\phi) dxdy$$

$$+ \int_{\Omega} |I - c_2|^2 (1 - H(\phi)) dxdy + \mu \int_{\Omega} |\nabla H(\phi)| dxdy. \tag{2.3}$$

Here, $H(\phi)$ and $\delta(\phi)$ are the one-dimensional Heaviside and Dirac function, respectively, and ϕ is the unknown level set function with the following properties:

$$
\begin{aligned}
\phi(x,y) &> 0, \quad (x,y) \in \text{in } (C) \\
\phi(x,y) &= 0, \quad (x,y) \in C \\
\phi(x,y) &< 0, \quad (x,y) \in \text{out } (C),
\end{aligned}
\tag{2.4}
$$

where in (C) and out (C) stand for the "inside" and "outside" regions divided by the curve C, respectively.

Minimizing the functional (2.3) with respect to ϕ is done by introducing an artificial time variable, and moving ϕ in the steepest descent direction to steady state:

$$
\frac{\partial \phi}{\partial t} = \delta(\phi) \left(-(I - c_1)^2 + (I - c_2)^2 + \mu \operatorname{div}\left(\frac{\nabla \phi}{|\nabla \phi|} \right) \right),
\tag{2.5}
$$

with initial conditions $\phi(0, x, y) = \phi_0(x, y)$, the signed distance function to the initial curve. In the above, c_1 and c_2 are, respectively, updated at each iteration by

$$
\begin{aligned}
c_1 &= \frac{\int_\Omega I(x,y) H(\phi(x,y)) dx dy}{\int_\Omega H(\phi(x,y)) dx dy}, \\
c_2 &= \frac{\int_\Omega I(x,y)(1 - H(\phi(x,y))) dx dy}{\int_\Omega (1 - H(\phi(x,y))) dx dy}.
\end{aligned}
\tag{2.6}
$$

The recovered image is a piecewise constant approximation to the image I.

Minimizing the functional (2.3) leads to a binary segmentation of the given image I: $I(x,y) \approx c_1 H(\phi(x,y)) + c_2(1 - H(\phi(x,y)))$. The C-V model has been generalized to the cases of more than two regions [13, 17, 23].

In practice, the Heaviside and Dirac functions $H(\phi)$ and $\delta(\phi)$ have to be approximated by smooth functions, which are typically defined by

$$
H_\varepsilon(\phi) = \frac{1}{2}\left(1 + \frac{2}{\pi} \arctan\left(\frac{\phi}{\varepsilon} \right) \right), \qquad \delta_\varepsilon(\phi) = H'_\varepsilon(\phi) = \frac{1}{\pi} \frac{\varepsilon^2}{\varepsilon^2 + \phi^2}.
\tag{2.7}
$$

The function $\delta_\varepsilon(\phi)$ is indeed an approximation to the Dirac function $\delta(\phi)$. To keep the notations simple, we still write $H(\phi)$ and $\delta(\phi)$ instead of $H_\varepsilon(\phi)$ and $\delta_\varepsilon(\phi)$ in what follows.

3. The Proposed Model

3.1. Description of Model

We use $L^{p(|\nabla I|)}$-norm instead of L^2-norm to define the external energy term of the C-V model, that is, the new external energy term is defined as

$$E_{ext}(c_1, c_2, \phi) = \int_\Omega |I - c_1|^{p(|\nabla I|)} H(\phi) dx dy + \int_\Omega |I - c_2|^{p(|\nabla I|)} (1 - H(\phi)) dx dy. \qquad (3.1)$$

The exponent $p(s): [0, +\infty) \rightarrow R$ is a monotonically increasing function with $2 < p(s) \leq K$, where K is a constant. A simple example is

$$p(s) = K - \frac{1}{8 + s^2}, \qquad (3.2)$$

where the constant $K > 17/8$ is tuned for a particular application. Clearly, $2 < p(s) \leq K$.

The external energy $E_{ext}(c_1, c_2, \phi)$ combines the gradient information with the region information; its role is to force the level set function to move towards the boundaries of the objects.

In order to control the smoothness of the zero level set $\{(x, y) \mid \phi(x, y) = 0\}$ and further avoid the occurrence of small isolated regions in the final segmentation, the regularization must be imposed on the zero level set:

$$\text{Length } \{\phi = 0\} = \int_\Omega |\nabla H(\phi)| dx dy = \int_\Omega \delta(\phi) |\nabla \phi| dx dy. \qquad (3.3)$$

In order to eliminate the need of the costly reinitialization procedure, we add an extra internal energy [7, 8],

$$P(\phi) = \int_\Omega \frac{1}{2} (|\nabla \phi| - 1)^2 dx dy, \qquad (3.4)$$

to the energy $E_{ext}(c_1, c_2, \phi)$ in (3.1). This energy actually serves as a metric to characterize how close the level set function is to a signed distance function.

Therefore, the total energy functional is given by

$$\begin{aligned} E(c_1, c_2, \phi) &= E_{ext}(c_1, c_2, \phi) + \mu \text{ Length } \{\phi = 0\} + \nu P(\phi) \\ &= \int_\Omega |I - c_1|^{p(|\nabla I|)} H(\phi) dx dy + \int_\Omega |I - c_2|^{p(|\nabla I|)} (1 - H(\phi)) dx dy \\ &\quad + \mu \int_\Omega \delta(\phi) |\nabla \phi| dx dy + \nu \int_\Omega \frac{1}{2} (|\nabla \phi| - 1)^2 dx dy. \end{aligned} \qquad (3.5)$$

Keeping ϕ fixed and minimizing the energy $E(c_1, c_2, \phi)$ with respect to the constants c_1 and c_2, we have

$$\int_\Omega |I(x,y) - c_1|^{p(|\nabla I|)-2}(I(x,y) - c_1)H(\phi)dxdy = 0,$$

$$\int_\Omega |I(x,y) - c_2|^{p(|\nabla I|)-2}(I(x,y) - c_2)(1 - H(\phi))dxdy = 0. \tag{3.6}$$

Since c_1 and c_2 do not have explicit expressions, we apply the fixed point algorithm to solve (3.6), namely,

$$c_1 = \frac{\int_\Omega |I(x,y) - c_1|^{p(|\nabla I|)-2}I(x,y)H(\phi)dxdy}{\int_\Omega |I(x,y) - c_1|^{p(|\nabla I|)-2}H(\phi)dxdy},$$

$$c_2 = \frac{\int_\Omega |I(x,y) - c_2|^{p(|\nabla I|)-2}I(x,y)(1 - H(\phi))dxdy}{\int_\Omega |I(x,y) - c_1|^{p(|\nabla I|)-2}(1 - H(\phi))dxdy}. \tag{3.7}$$

Keeping c_1 and c_2 fixed, and minimizing the functional (3.5) with respect to ϕ by the gradient descent, yields the associated Euler-Lagrange equation for ϕ as follows:

$$\frac{\partial \phi}{\partial t} = \delta(\phi)\left[\mu \operatorname{div}\left(\frac{\nabla \phi}{|\nabla \phi|}\right) - |I - c_1|^{p(|\nabla I|)} + |I - c_2|^{p(|\nabla I|)}\right] + \nu\left(\Delta \phi - \operatorname{div}\left(\frac{\nabla \phi}{|\nabla \phi|}\right)\right), \tag{3.8}$$

with the initial and Neumann boundary conditions:

$$\phi(x,y,0) = \phi_0(x,y), \quad \frac{\partial \phi}{\partial \vec{n}} = 0 \text{ on } \partial\Omega, \tag{3.9}$$

where $\vec{n}$ denotes the exterior normal to the boundary $\partial\Omega$ and $\partial\phi/\partial\vec{n}$ denotes the normal derivative of ϕ at the boundary.

3.2. Why Use $L^{p(|\nabla I|)}$-Norm Instead of L^2-Norm?

Since the image domain Ω is bounded and $2 < p(|\nabla I|) \leq K$, it is well known that $L^{p(|\nabla I|)}(\Omega) \subset L^2(\Omega)$ with $\|u\|_{L^2} \leq M\|u\|_{L^{p(|\nabla I|)}}$, where M is a positive constant. In fact, by simple proof, we obtain M, that is, $M = (|\Omega|)^{(K-2/2K)}$, and it is independent of image intensity. That is to say, the $L^{p(|\nabla I|)}$ norm $\|\cdot\|_{L^{p(|\nabla I|)}} (p(|\nabla I|) > 2)$ is stronger than the L^2 norm $\|\cdot\|_{L^2}$.

The external energy term in (3.5) can be rewritten as

$$\int_\Omega |I - c_1|^{p(|\nabla I|)} H(\phi) dxdy + \int_\Omega |I - c_2|^{p(|\nabla I|)} (1 - H(\phi)) dxdy$$

$$= \int_{\{\phi>0\}} |I(x,y) - c_1|^{p(|\nabla I|)} dxdy + \int_{\{\phi<0\}} |I(x,y) - c_2|^{p(|\nabla I|)} dxdy \qquad (3.10)$$

$$= \int_\Omega |I(x,y) - c_1 H(\phi) - c_2(1 - H(\phi))|^{p(|\nabla I|)} dxdy,$$

thus minimizing this external energy term with respect to ϕ leads to the optimal binary segmentation of the given image I:

$$I(x,y) \approx I_{p(|\nabla I|)}(x,y) = c_1 H(\phi_{p(|\nabla I|)}(x,y)) + c_2(1 - H(\phi_{p(|\nabla I|)}(x,y))), \qquad (3.11)$$

in the sense of the $L^{p(|\nabla I|)}$ norm, where $\phi_{p(|\nabla I|)}(x,y)$ is a minimizer of the external energy. Because the $L^{p(|\nabla I|)}(p(|\nabla I|) > 2)$ is stronger than the L^2 norm, we have

$$\int_\Omega |I(x,y) - I_2(x,y)|^2 dxdy \leq M \int_\Omega |I(x,y) - I_{p(|\nabla I|)}(x,y)|^{p(|\nabla I|)} dxdy. \qquad (3.12)$$

This implies that the binary image $I_{p(|\nabla I|)}(x,y)(p(|\nabla I|) > 2)$ better approximates the original image $I(x,y)$ than the binary image $I_2(x,y)$. When the original image $I(x,y)$ approximates the $I_{p(|\nabla I|)}(x,y)$, the speed of external energy term that approximates zero in the sense of $L^{p(|\nabla I|)}(p(|\nabla I|) > 2)$ norm is much faster than the speed in the sense of L^2 norm. Therefore, the segmentation speed of the proposed model is much faster than the C-V model.

On the other hand, the variable exponent $p(|\nabla I|)$ reflects the local property of image, and so the proposed model adapts the exponent to fit the image information automatically. Therefore, the proposed model with $p(|\nabla I|) > 2$ can force the level set function to move towards the boundaries of the objects adaptively, and it has the hope of segmenting those images with low contrast and blurred boundaries.

Next, we use the experiment to show that the use of $p(|\nabla I|) > 2$ in $L^{p(|\nabla I|)}$-norm can achieve satisfactory segmentation results for those images with noise and low contrast. However, the use of $p(|\nabla I|) = 2$ fails to handle those images. At the same time, these results also show that the proposed model with $p(|\nabla I|) > 2$ can segment objects with blurred boundaries.

Figure 1 demonstrates the segmentation results using $p(|\nabla I|) = 2$ and $p(|\nabla I|) > 2$, respectively, for three infrared images (left to right) with high noise (105×144, 159×163) and low contrast (159×165). To make a fair comparison, we choose the best parameter μ (given in the caption) and contour initialization for $p(|\nabla I|) = 2$. And we choose the same value of μ for both cases. The segmentation results of both cases are shown in the top row ($p(|\nabla I|) = 2$) and bottom row ($p(|\nabla I|) > 2$), respectively. This experiment shows that the use of $p(|\nabla I|) > 2$ rather than $p(|\nabla I|) = 2$ can really segment the infrared images with noise and low contrast accurately. It should be pointed out that all other different initial curves give the same segmentation results only in a single iteration in the case of $p(|\nabla I|) > 2$ for these images.
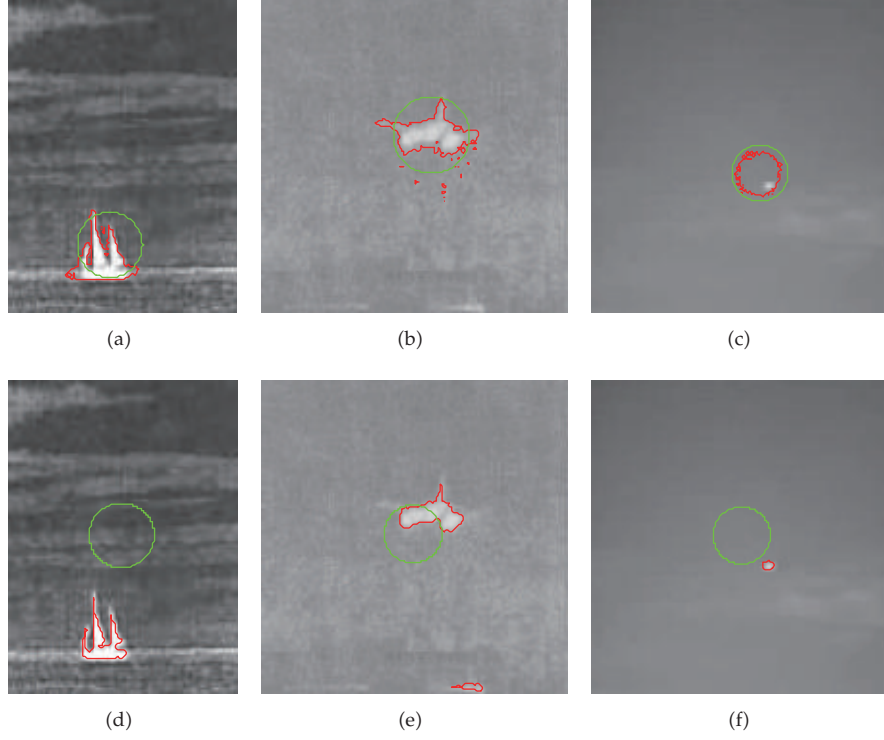
Figure 1: Results of our model with $p(|\nabla I|) = 2$ and $p(|\nabla I|) > 2$ for three infrared images with noise (the first two images) and low contrast (the last image), (left to right: $\mu = 0.09 \times 255 \times 255, 0.001 \times 255 \times 255, 0.1 \times 255 \times 255$), where initial and final contours are shown in green and red, respectively. Top row: $p(|\nabla I|) = 2$, at the 75, 100, 50 iterations. Bottom row: $p(|\nabla I|) > 2$ ($K = 5.2, 4.1, 6.4$), at the 1st iteration.

4. Implementation and Experimental Results

4.1. Numerical Algorithm

In this subsection, we briefly present the numerical scheme to solve the proposed model. We recall first the notations in the finite difference scheme. Let τ, Δt, and $(x_i, y_j) = (i\tau, j\tau)$ be the space step, the time step, and the grid points, respectively.

Let $\phi_{i,j}^n = \phi_{i,j}^n(x_i, y_j, n\Delta t)$ be an approximation of the level set function $\phi(x, y, t)$ with $n \geq 0$, $\phi^0 = \phi_0$, where ϕ_0 is the initial level set function. The central differences of spatial partial derivatives are expressed in the following notations:

$$\Delta^x \phi_{i,j} = \frac{\phi_{i+1,j} - \phi_{i-1,j}}{2\tau}, \qquad \Delta^y \phi_{i,j} = \frac{\phi_{i,j+1} - \phi_{i,j-1}}{2\tau}. \tag{4.1}$$

Then, the numerical approximation to (3.8) can be simply written as

$$\frac{\phi_{i,j}^{n+1} - \phi_{i,j}^n}{\Delta t} = \delta_\varepsilon\left(\phi_{i,j}^n\right)\left(\mu k_{i,j}^n - \left|I_{i,j} - c_1^{n+1}\right|^{p(|\nabla I|)} + \left|I_{i,j} - c_2^{n+1}\right|^{p(|\nabla I|)}\right)$$
$$+ \nu\left(\Delta^x\left(\Delta^x \phi_{i,j}^n\right) + \Delta^y\left(\Delta^y \phi_{i,j}^n\right) - k_{i,j}^n\right), \tag{4.2}$$

where

$$k_{i,j}^n = \Delta^x \left(\frac{\Delta^x \phi_{i,j}^n}{\sqrt{\left(\Delta^x \phi_{i,j}^n\right)^2 + \left(\Delta^y \phi_{i,j}^n\right)^2 + \eta}} \right) + \Delta^y \left(\frac{\Delta^y \phi_{i,j}^n}{\sqrt{\left(\Delta^x \phi_{i,j}^n\right)^2 + \left(\Delta^y \phi_{i,j}^n\right)^2 + \eta}} \right). \quad (4.3)$$

In summary, the main procedures of the improved algorithm are as follows.

(1) Initialize the level set function $\phi^0(x, y) = \phi_0(x, y)$, and compute the initial values c_1^0 and c_2^0 by (2.6) and variable exponent $p(|\nabla I|)$ by (3.2), and then set $n = 0$.

(2) Compute the values c_1^{n+1} and c_2^{n+1} using

$$c_1^{n+1} = \frac{\int_\Omega |I(x,y) - c_1^n|^{p(|\nabla I|)-2} I(x,y) H(\phi^n) dx dy}{\int_\Omega |I(x,y) - c_1^n|^{p(|\nabla I|)-2} H(\phi^n) dx dy},$$

$$c_2^{n+1} = \frac{\int_\Omega |I(x,y) - c_2^n|^{p(|\nabla I|)-2} I(x,y) (1 - H(\phi^n)) dx dy}{\int_\Omega |I(x,y) - c_2^n|^{p(|\nabla I|)-2} (1 - H(\phi^n)) dx dy}.$$

$$(4.4)$$

(3) Evolve the level set function by solving (4.2) to obtain $\phi^{n+1}(x, y)$.

(4) If the zero level set of $\phi^{n+1}(x, y)$ is exactly on the object boundary, then stop; otherwise, let $n = n + 1$, then return to step (2).

4.2. Experimental Results

We carry out several experiments on some synthetic and real images to demonstrate the performance of the proposed model. To make fair comparison, for the C-V model we added the internal energy (3.4) into the functional (2.3) to avoid the reinitialization step. For all experiments, the level set function for C-V model is initialized to the signed distance function to a circle in image domain; and for both RSF model and the proposed model, the initial level set function ϕ is simply chosen as a binary step function as in [7, 8], which takes a positive constant value ρ inside a region $R_0 \subset \Omega$ and a negative constant value $-\rho$ outside R_0. We choose $\rho = 1$ for all experiments in this paper.

Unless otherwise specified, we use the following default setting of the parameters for all the experiments: $\tau = 1$, $\Delta t = 0.1$, $\mu = 0.001 \times 255 \times 255$, $\nu = 0.04$, and $\varepsilon = 1$ (for $\delta_\varepsilon(z)$). For the proposed model, in all experiments, the initial contours are chosen as circles with radius of fifteen (excluding Figures 3–5), located at the centre of image domain. In general, we choose the parameter K ranging from 2.2 to 7 in the proposed model. The full decision of value K depends on varied image scenes. We will give the exact value of K each time.

The first four experiments show the segmentation results of both the proposed model and C-V model for some synthetic and real images.

Figure 2 shows the segmentation results of both models for five synthetic images. As can be seen, the proposed model obtains the satisfactory segmentation results for these images (left to right: $K = 2.7, 2.7, 2.8, 3,$ and 2.9), which are almost the same as C-V model visually. Table 1 gives the CPU times and iteration numbers of both models. We can observe that both CPU times and iteration numbers of the proposed model are less than C-V model.
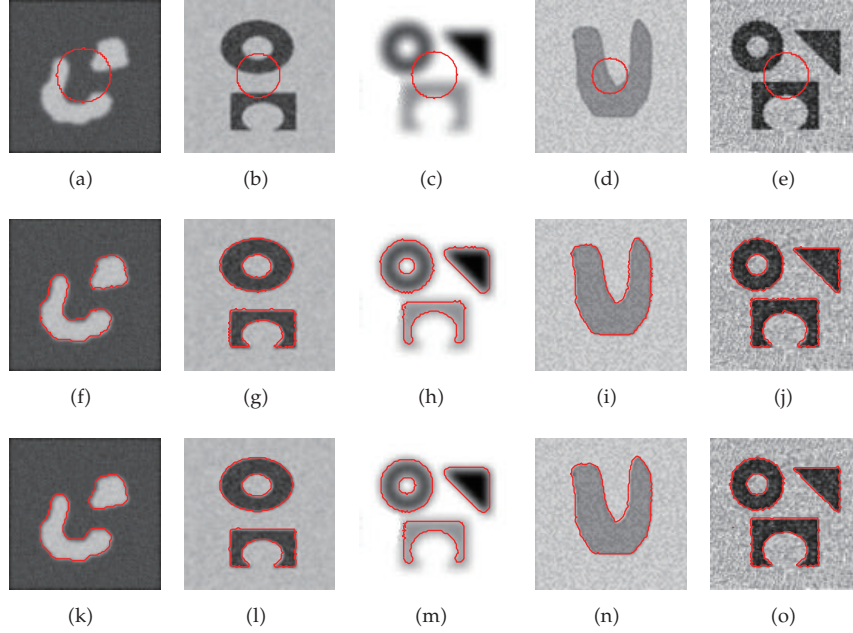
Figure 2: Segmentation results of both models for five synthetic images. Upper row: initial contours. Middle row: C-V model. Lower row: proposed model.

Table 1: CPU times (in seconds) and iteration numbers in Figure 2

Image ID	(a)	(b)	(c)	(d)	(e)
Image size	84×84	102×103	100×100	128×128	100×99
C-V model	0.5005	2.5693	9.4127	15.3524	4.7347
Iteration numbers	10	50	200	245	100
Proposed model	0.0701	0.0809	0.0785	0.0937	0.0794
Iteration numbers	1	1	1	1	1

Figures 3 and 4 demonstrate that the segmentation results of both models for a medical image (112×66), and an aerial image (128×128) with five initial circles of different positions. For the proposed model, we choose only a parameter K for all different positions ($K = 3.3$ in Figure 3 and $K = 3.2$ in Figure 4), all those different initial curves give the same segmentation results in a single iteration. However, by inspecting these images carefully, we can see that only one initial curve gives accurate segmentation results by the C-V model (see the last image in middle row of Figure 3 and the third image in middle row of Figure 4); and this shows that the C-V model is, to some extent, sensitive to the position of initial curve.

Figure 5 shows the segmentation results of C-V model, RSF model, and the proposed model for a noisy infrared image with four initial circles of different positions and sizes. For the proposed model, we simply choose a fixed $K = 3.6$ for all those different initial curves and give the same segmentation results in a single iteration, as shown in the lower row of Figure 5. However, we observe from the second and third rows that only one initial curve gives correct segmentation results by both C-V model and RSF model. This shows that both C-V model and RSF model are, to some extent, sensitive to the initial circles of different positions and sizes.

The next five experiments show the segmentation results of Bresson et al.'s model [18], Goldstein et al.'s model [20], and the proposed model for some real images. To make a fair
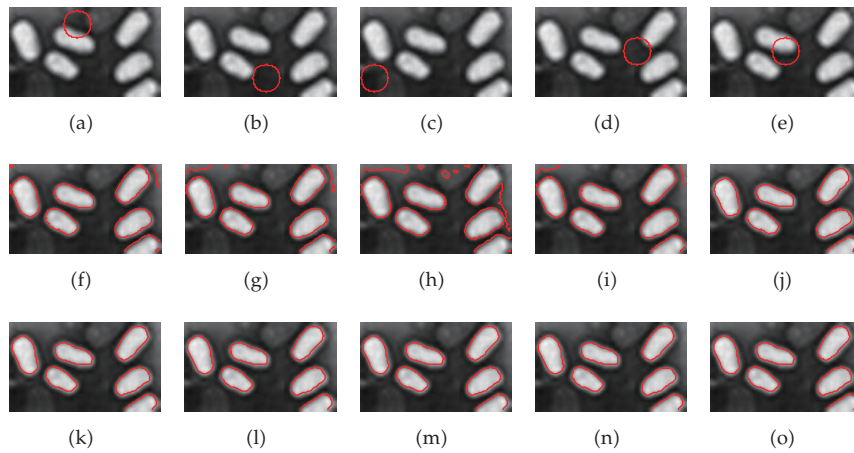
Figure 3: Applications of both models to a real medical image. Upper row: initial contours. Middle row: C-V model, (left to right) after 1000, 1000, 1500, 1000, and 100 iterations. Lower row: proposed model, at the 1st iteration.
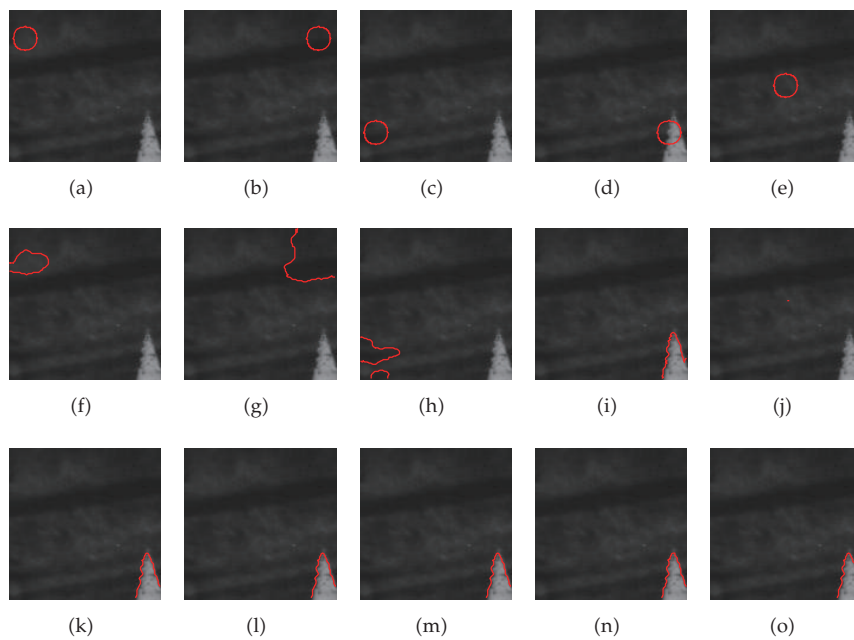

Figure 4: Applications of both models to an aerial image. Upper row: initial contours. Middle row: C-V model, (left to right) after 500, 500, 500, 15, and 220 iterations. Lower row: proposed model, at the 1st iteration.

comparison, we choose the best parameters for both Bresson et al.'s model and Goldstein et al.'s model.

In Figure 6, we apply the three models to four infrared images with low contrast and blurred boundaries. The test images are of size 150×56, 158×167, 159×165, and 159×166, which are shown in the first column of Figure 6. For such images, both Bresson et al.'s model and Goldstein et al.'s model show erroneous results, as shown in the second
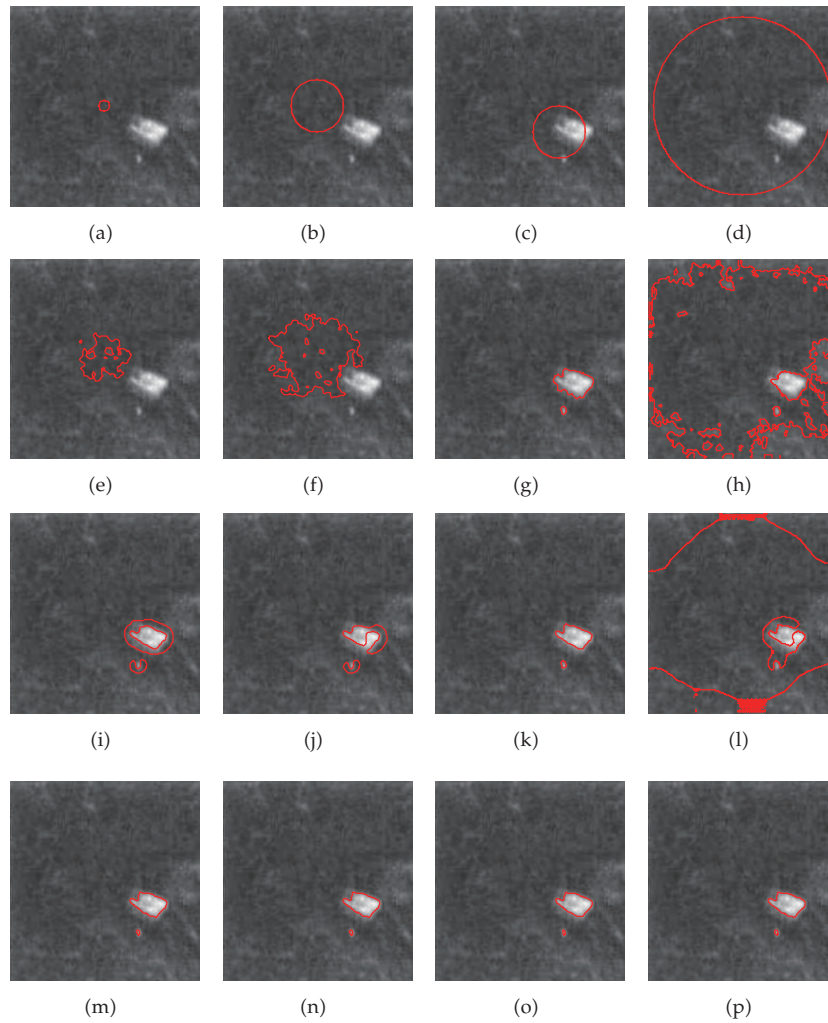
Figure 5: Segmentation results of three models for a noisy infrared image. Top row: initial contours. The second row: C-V model, after 500, 500, 105, and 500 iterations. The third row: RSF model, after 150, 500, 210, and 500 iterations. Bottom row: proposed model, at the 1st iteration.

and third columns of Figure 6. In fact, no matter how many iterations, some part of the background/foreground is incorrectly identified as the foreground/background. Due to the introduction of $L^{p(|\nabla I|)}(p(|\nabla I|) > 2)$ norm in the proposed model, by alternating $K = 6.6, 6.5, 6.4,$ and 5, the proposed model successfully detects the objects for all these images; see the last column of Figure 6.

Figure 7 shows the detective results of three models for three aerial images with low contrast and blurred boundaries (128×128). For the proposed model, we simply choose a fixed $K = 4.4$ for all these images. We clearly observe from Figure 7 that both the Bresson et al.'s model and the proposed model can achieve the satisfactory detective results for these images, while Goldstein et al.'s model fails to handle them. Besides, from Table 2, we can see that CPU times of the proposed model are very small compared to Bresson et al.'s model.
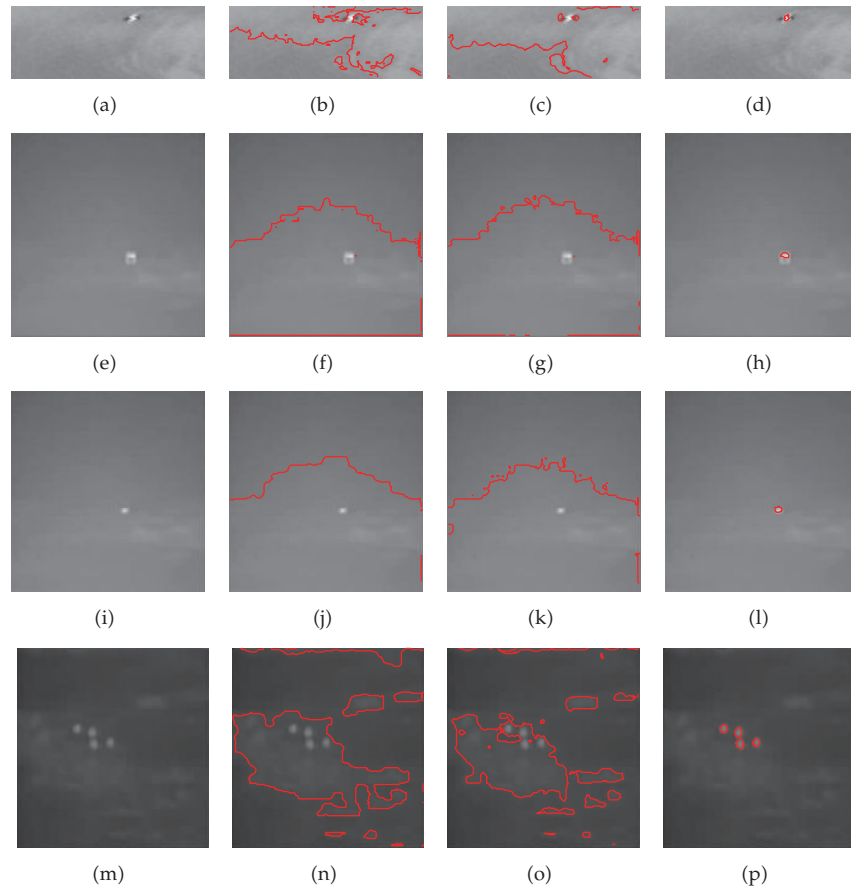
(a) (b) (c) (d)

(e) (f) (g) (h)

(i) (j) (k) (l)

(m) (n) (o) (p)

Figure 6: Detective results of three models for four infrared images with low contrast and blurred boundaries. The first column: original images. The second column: Bresson et al.'s model. The third column: Goldstein et al.'s model. The last column: proposed model, at the 1st iteration.

Table 2: CPU times (in seconds) in Figure 7.

Image ID	(a)	(e)	(i)
Bresson et al.'s model	8.3615	0.7826	0.7629
Proposed model	0.0908	0.0888	0.0887

In Figure 8, we consider three range images of saddle and cone with step or roof edges (top to bottom: 287×287, 290×290, and 285×282), these of which are taken from that in [16]. The top row of Figure 8 is the segmentation of a saddle range image. This range image has complicated image intensity distribution, in which the end boundaries of the saddle are step edges, and the side boundaries are roof edges. The last two rows of Figure 8 are the segmentation results of two cones range images. The boundaries between the cones and the bottom planes are roof edges. As can be seen from the last two columns of Figure 8 that the objects are accurately extracted by the Goldstein et al.'s model and the proposed model (top to bottom: $K = 2.9, 2.4,$ and 2.2). However, by carefully inspecting these images in the second column, Bresson et al.'s model cannot extract the real object boundaries, which leads
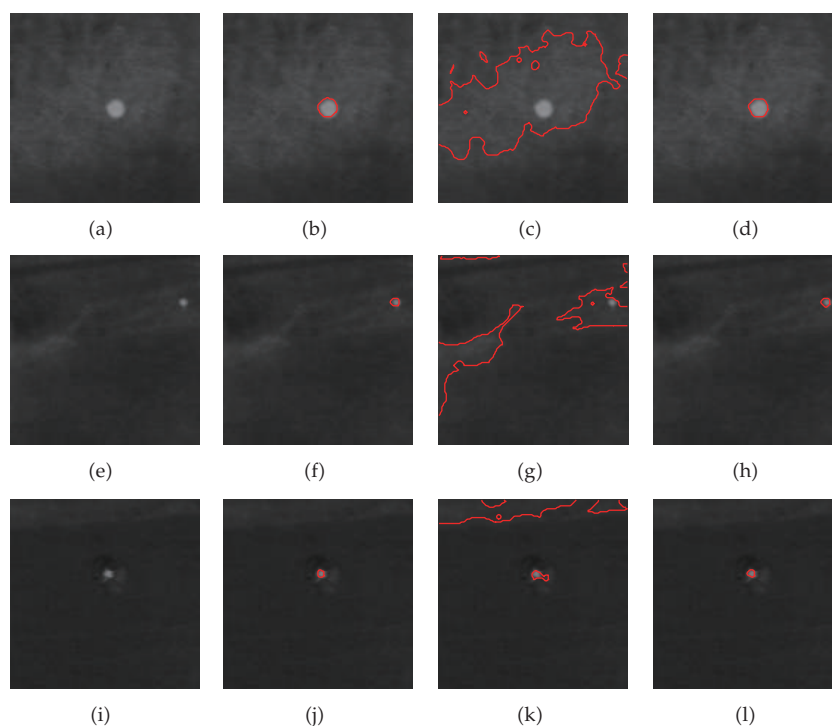
(a)	(b)	(c)	(d)
(e)	(f)	(g)	(h)
(i)	(j)	(k)	(l)

Figure 7: Detective results of three models for aerial images with low contrast and blurred boundaries. The first column: original images. The second column: Bresson et al.'s model. The third column: Goldstein et al.'s model. The last column: proposed model, at the 1st iteration.

Table 3: CPU times (in seconds) in Figure 8.

Image ID	(a)	(e)	(i)
Goldstein et al.'s model	0.0310	0.0470	0.1720
Proposed model	0.2826	0.2858	0.2719

to the boundary leakage. Here, we notice that the proposed model needs more CPU the times than Goldstein et al.'s model (see Table 3).

Figures 9 and 10 show the segmentation results of the three models for six real images. The test images are six images, in which four images are shown in the first row of Figure 9 (left to right: 236×195, 135×125, 94×123, and 233×233) and two images are shown in the first column of Figure 10 (128×128, 275×203). We choose $K = 2.6, 2.9, 3.7$, and 3.4 for these images in Figure 9, and $K = 3.3, 2.5$ for the two images in Figure 10. As can be seen from Figures 9 and 10 that the three models can obtain satisfactory segmentation results for all these images. Besides, we observe from Tables 4 and 5 that the CPU times of the proposed model are less than the Bresson et al.'s model [18], but more than the Goldstein et al.'s model [20].

The last experiment shows the segmentation results for four medical images with low contrast and blurred boundaries using C-V model, Bresson et al.'s model, Goldstein et al.'s model, and the proposed model. The test images, shown in the top row of Figure 11, (left to right) are two real images of digital mammography (158×151, 168×147), a real corpus callosum MR image (170×126) and a heart image (238×233). For the third image, the object is to segment the blurry corpus callosum region which is surrounded by the dim

(a)   (b)   (c)   (d)

(e)   (f)   (g)   (h)

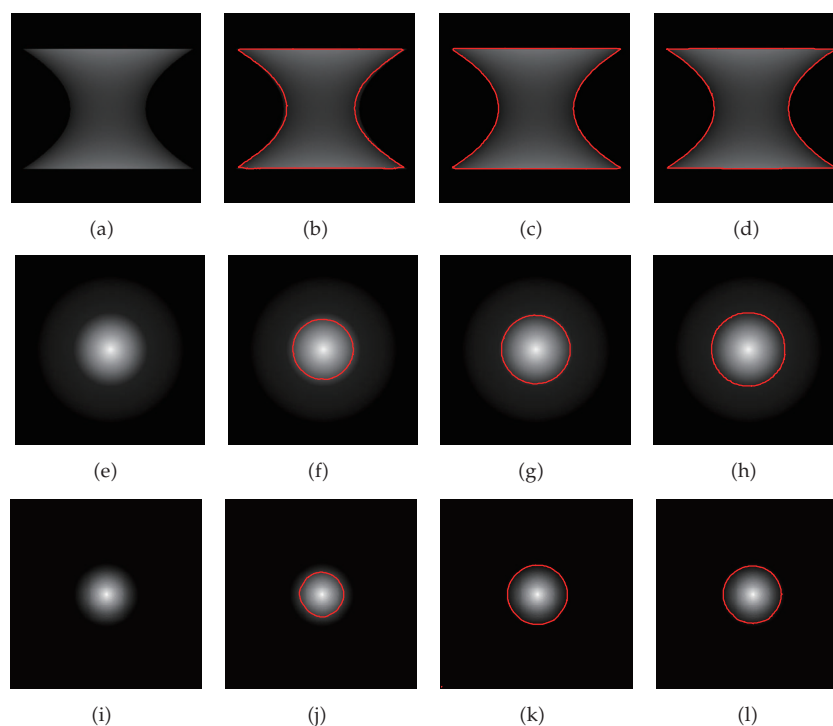(i)   (j)   (k)   (l)

Figure 8: Segmentation results of three models for three range images. The first column: original images. The second column: Bresson et al.'s model. The third column: Goldstein et al.'s model. The last column: proposed model, at the 1st iteration.

Table 4: CPU times (in seconds) in Figure 9.

Image ID	(a)	(b)	(c)	(d)
Bresson et al.'s model	0.3878	0.2821	0.4696	0.2338
Goldstein et al.'s model	0.0150	0.0150	0.0160	0.0470
Proposed model	0.1721	0.0935	0.0820	0.1864

Table 5: CPU times (in seconds) in Figure 10.

Image ID	(a)	(e)
Bresson et al.'s model	0.2429	0.8226
Goldstein et al.'s model	0.0160	0.0150
Proposed model	0.1731	0.3968

brain tissues. For the heart image, the desired result is to capture the bright ventricle. For all images, segmentation of objects of interests is difficult because of low contrast and blurred boundaries. To make a fair comparison, we choose the best parameters for the two models (Bresson et al.'s model and Goldstein et al.'s model) and contour initialization for C-V model, and $K = 5, 5.4, 5.6,$ and 5.8 for the proposed model. We observe from the second row that the C-V model cannot segment them correctly, in which appears some noise points around objects. The last three rows show that Bresson et al.'s model successfully extracts the objects only for the first two images and Goldstein et al.'s model only segments the first image
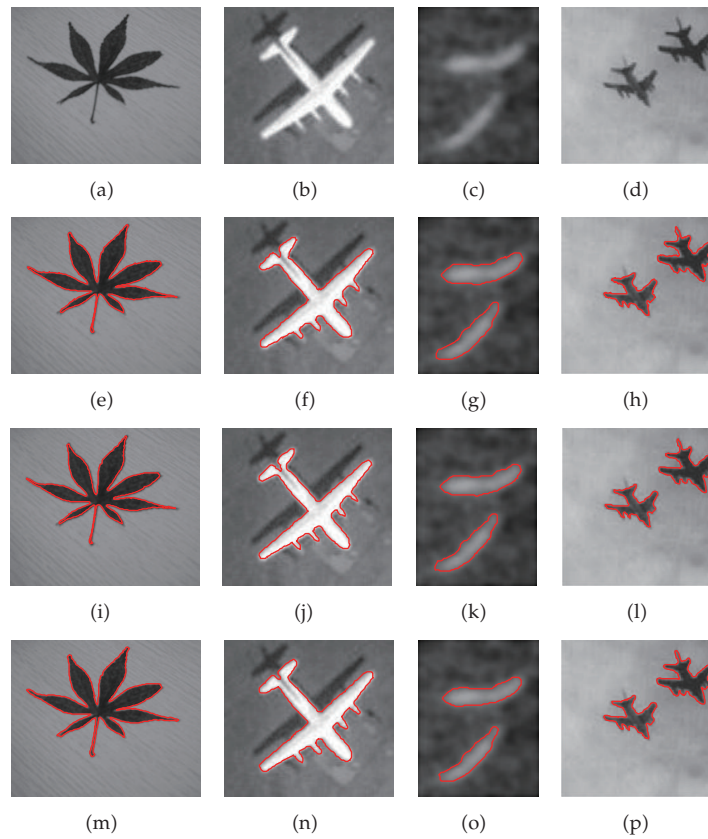
Figure 9: Applications of three models to four real images. Top row: original images. The second row: Bresson et al.'s model. The third row: Goldstein et al.'s model. Bottom row: proposed model, at the 1st iteration.
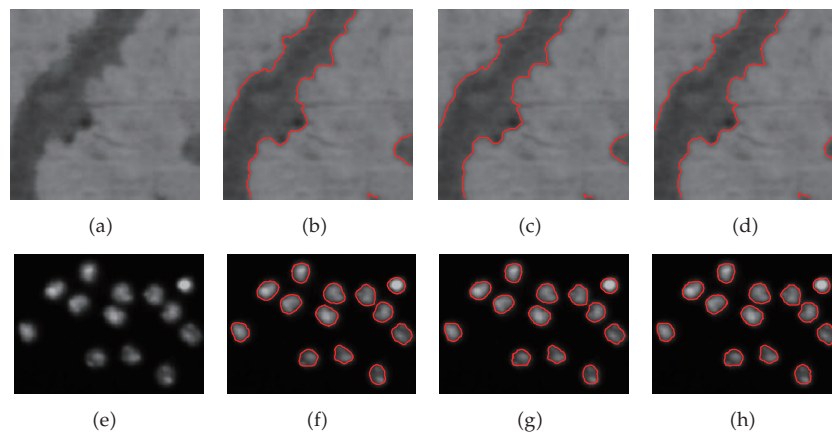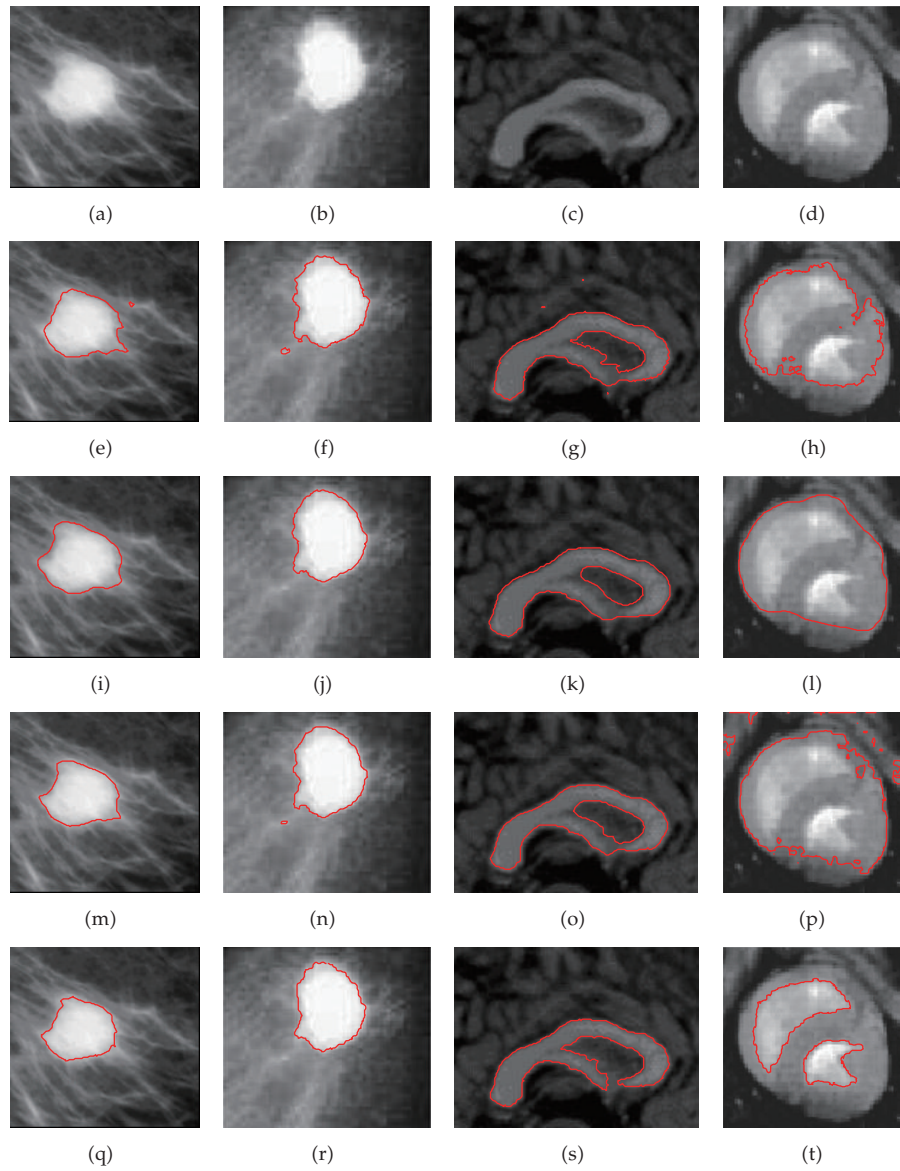

Figure 10: Applications of three models to two real images with multiple objects. The first column: Original images. The second column: Bresson et al.'s model. The third column: Goldstein et al.'s model. The last column: Proposed model, at the 2nd iteration.

Figure 11: Results of four models for four medical images with low contrast and blurred boundaries. Top row: original images. The second row: C-V model. The third row: Bresson et al.'s model. The fourth row: Goldstein et al.'s model. Bottom row: proposed model, at the 1st iteration.

Table 6: CPU times (in seconds) in Figure 11.

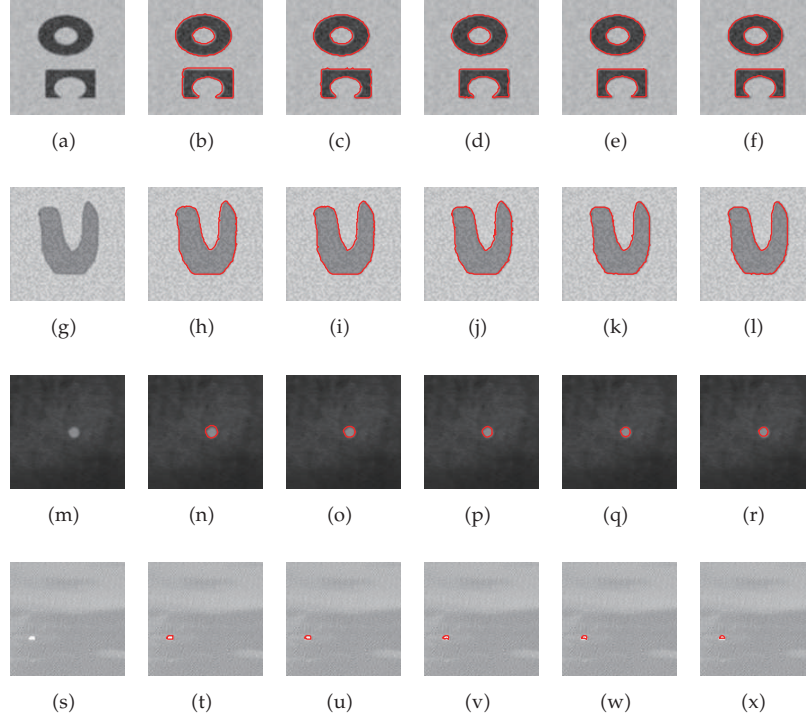| Image ID	(a)	(b)	(c)	(d)
Bresson et al.'s model	3.8406	2.9298	—	—
Goldstein et al.'s model	0.1880	—	—	—
Proposed model	0.1053	0.1105	0.1018	0.2007

Figure 12: Results of the proposed model with different K for two synthetic images and two real images, at the 1st iteration. (left to right) (a) Original image, (b)–(f) K = 2.2, 2.6, 2.8, 3.2, and 3.4. (g) Original image, (h)–(l) K = 2.5, 2.8, 3.1, 3.4, and 3.7. (m) Original image, (n)–(r) K = 4.1, 4.5, 4.9, 5.2, and 5.5. (s) Original image, (t)–(x) K = 5.7, 6, 6.3, 6.6, and 7.

correctly, while the proposed model effectively and quickly extracts objects for all images in a single iteration. Besides, the proposed model needs less CPU times than both Bresson et al.'s model and Goldstein et al.'s model (see Table 6).

5. Dissussion

In this section, we simply discuss about the parameter K. For the proposed model, K for the function $p(|\nabla I|)$ is very important to the segmentation results. Theoretically, if K is larger, then the $p(|\nabla I|)$ norm is stronger. That is to say, when larger K is served as external energy term for the proposed model, there have been better approximation effects for those images with low contrast and blurred boundaries. Here, we discuss the setting of K when it is chosen by hand as some fixed value. Experimentally, our observations are as follows: K is typically chosen as a constant between 2.2 and 7. For synthetic images and range images, we choose K in the range between 2.2 and 3; for aerial images and some medical images (excluding Figure 10(e)), we choose K in the range between 3.1 and 4.9; for infrared images and those medical images with low contrast and blurred boundaries, we choose K in the range between 5 and 7.

It is worth emphasizing that the proposed model is robust to K. For this purpose, we apply the proposed model to two synthetic images (102×103, 128×128) and two real images (128×128, 128×128), (top to bottom) as shown in the first column of Figure 12. For each image,

we choose default initial contour, and all those different K give the almost same segmentation results in a single iteration, as shown in Figures 12(b), 12(c), 12(d), 12(e), 12(f), 12(h), 12(i), 12(j), 12(k), 12(l), 12(n), 12(o), 12(p), 12(q), 12(r), 12(t), 12(u), 12(v), 12(w) and 12(x).

6. Conclusion

In this paper, following the well-known C-V model we propose a region-based implicit active contour model based on $L^{p(|\nabla I|)}(p(|\nabla I|) > 2)$ norm for images segmentation. First, the proposed model shares the advantages of the C-V model, such as the robustness to noise and the location of initial contours, and allows us to segment those images that the C-V model can handle (but the segmentation speed of the proposed model is much faster than C-V model). Second, due to the function $p(|\nabla I|)$ fits the gradient information, the proposed model can effectively and quickly segment those images with low contrast and blurred boundaries. It should be pointed out that the segmentation speed of the proposed model is faster than Bresson et al.'s model [18], but it is lower than Goldstein et al.'s model [20]. In the future, we will introduce Split Bregman method to the proposed model.

Acknowledgments

References

[1] S. Osher and N. Paragios, *Geometric Level Set Methods in Imaging, Vision, and Graphics*, Springer, New York, NY, USA, 2003.

[2] B. B. Kimia, A. R. Tannenbaum, and S. W. Zucker, "Shapes, shocks, and deformations I: the components of two-dimensional shape and the reaction-diffusion space," *International Journal of Computer Vision*, vol. 15, no. 3, pp. 189–224, 1995.

[3] S. Osher and R. Fedkiw, *Level Set Methods and Dynamic Implicit Surfaces*, vol. 153 of *Applied Mathematical Sciences*, Springer, New York, NY, USA, 2003.

[4] M. Kass, A. Witkin, and D. Terzopoulos, "Snakes: active contour models," *International Journal of Computer Vision*, vol. 1, no. 4, pp. 321–331, 1988.

[5] V. Caselles, F. Catté, T. Coll, and F. Dibos, "A geometric model for active contours in image processing," *Numerische Mathematik*, vol. 66, no. 1, pp. 1–31, 1993.

[6] V. Caselles, R. Kimmel, and G. Sapiro, "Geodesic Active Contours," *International Journal of Computer Vision*, vol. 22, no. 1, pp. 61–79, 1997.

[7] C. Li, C. Xu, C. Gui, and M. D. Fox, "Level set evolution without re-initialization: a new variational formulation," in *Proceedings of the IEEE Computer Society Conference on Computer Vision and Pattern Recognition (CVPR '05)*, vol. 1, pp. 430–436, San Diego, Calif, USA, June 2005.

[8] C. Li, C. Xu, C. Gui, and M. D. Fox, "Distance regularized level set evolution and its application to image segmentation," *IEEE Transactions on Image Processing*, vol. 19, no. 12, pp. 3243–3254, 2010.

[9] M. Li, C. He, and Y. Zhan, "Adaptive level-set evolution without initial contours for image segmentation," *Journal of Electronic Imaging*, vol. 20, no. 2, Article ID 023004, 2011.

[10] M. Li, C. He, and Y. Zhan, "Adaptive regularized level set method for weak boundary object segmentation," *Mathematical Problems in Engineering*, vol. 2012, Article ID 369472, 16 pages, 2012.

[11] T. F. Chan and L. A. Vese, "Active contours without edges," *IEEE Transactions on Image Processing*, vol. 10, no. 2, pp. 266–277, 2001.

[12] C. Li, C. Y. Kao, J. C. Gore, and Z. Ding, "Minimization of region-scalable fitting energy for image segmentation," *IEEE Transactions on Image Processing*, vol. 17, no. 10, pp. 1940–1949, 2008.

[13] L. A. Vese and T. F. Chan, "A multiphase level set framework for image segmentation using the Mumford and Shah model," *International Journal of Computer Vision*, vol. 50, no. 3, pp. 271–293, 2002.

[14] S. Gao and T. D. Bui, "A new image segmentation and smoothing model," in *Proceedings of the 2nd IEEE International Symposium on Biomedical Imaging: Macro to Nano*, vol. 1, pp. 137–140, April 2004.

[15] K. Zhang, H. Song, and L. Zhang, "Active contours driven by local image fitting energy," *Pattern Recognition*, vol. 43, no. 4, pp. 1199–1206, 2010.

[16] X. Du and T. D. Bui, "A new model for image segmentation," *IEEE Signal Processing Letters*, vol. 15, pp. 182–185, 2008.

[17] G. Chung and L. A. Vese, "Image segmentation using a multilayer level-set approach," *Computing and Visualization in Science*, vol. 12, no. 6, pp. 267–285, 2009.

[18] X. Bresson, S. Esedoglu, P. Vandergheynst, J. P. Thiran, and S. Osher, "Fast global minimization of the active contour/snake model," *Journal of Mathematical Imaging and Vision*, vol. 28, no. 2, pp. 151–167, 2007.

[19] T. F. Chan, S. Esedoglu, and M. Nikolova, "Algorithms for finding global minimizers of image segmentation and denoising models," *SIAM Journal on Applied Mathematics*, vol. 66, no. 5, pp. 1632–1648, 2006.

[20] T. Goldstein, X. Bresson, and S. Osher, "Geometric applications of the Split Bregman method: segmentation and surface reconstruction," *Journal of Scientific Computing*, vol. 45, no. 1–3, pp. 272–293, 2010.

[21] D. Mumford and J. Shah, "Optimal approximations by piecewise smooth functions and associated variational problems," *Communications on Pure and Applied Mathematics*, vol. 42, no. 5, pp. 577–685, 1989.

[22] J.-M. Morel and S. Solimini, *Variational Methods in Image Segmentation*, Progress in Nonlinear Differential Equations and Their Applications No.14, Birkhäuser, Boston, Mass, USA, 1995.

[23] E. Bae and X. C. Tai, "Efficient global minimization for the multiphase Chan-Vese model of image segmentation," in *Proceedings of the 7th International Conference on Energy Minimization Methods in Computer Vision and Pattern Recognition (EMMCVPR '09)*, vol. 5681 of *Lecture Notes in Computer Science*, pp. 28–41, 2009.